## MICROROBOTS

# Submillimeter-scale multimaterial terrestrial robots

Mengdi Han[1]†, Xiaogang Guo[2,3]†, Xuexian Chen[4]†, Cunman Liang[5], Hangbo Zhao[6,7], Qihui Zhang[8], Wubin Bai[6,8], Fan Zhang[3], Heming Wei[9], Changsheng Wu[6], Qinghong Cui[1], Shenglian Yao[6,10], Bohan Sun[6,11], Yiyuan Yang[12], Quansan Yang[12], Yuhang Ma[13], Zhaoguo Xue[3], Jean Won Kwak[6,12], Tianqi Jin[3], Qing Tu[14], Enming Song[15], Ziao Tian[16], Yongfeng Mei[17], Daining Fang[2], Haixia Zhang[4], Yonggang Huang[8,12,18]*, Yihui Zhang[3]*, John A. Rogers[6,8,12,19,20,21,22]*

Robots with submillimeter dimensions are of interest for applications that range from tools for minimally invasive surgical procedures in clinical medicine to vehicles for manipulating cells/tissues in biology research. The limited classes of structures and materials that can be used in such robots, however, create challenges in achieving desired performance parameters and modes of operation. Here, we introduce approaches in manufacturing and actuation that address these constraints to enable untethered, terrestrial robots with complex, three-dimensional (3D) geometries and heterogeneous material construction. The manufacturing procedure exploits controlled mechanical buckling to create 3D multimaterial structures in layouts that range from arrays of filaments and origami constructs to biomimetic configurations and others. A balance of forces associated with a one-way shape memory alloy and the elastic resilience of an encapsulating shell provides the basis for reversible deformations of these structures. Modes of locomotion and manipulation span from bending, twisting, and expansion upon global heating to linear/curvilinear crawling, walking, turning, and jumping upon laser-induced local thermal actuation. Photonic structures such as retroreflectors and colorimetric sensing materials support simple forms of wireless monitoring and localization. These collective advances in materials, manufacturing, actuation, and sensing add to a growing body of capabilities in this emerging field of technology.

## INTRODUCTION

Many of the most advanced, large-scale robots incorporate complex functions and motion modalities, sometimes in bioinspired three-dimensional (3D) designs and with heterogeneous collections of materials. Examples of the former include systems that resemble arthropods or vertebrates (1–5); those of the latter include soft, hydraulically/pneumatically actuated material structures with rigid structural supports (6–8). In both cases, electronics/optoelectronics components and power supply systems support sensing, control, and communication (9–11). Miniaturization of such types of bioinspired robots to millimeter or submillimeter dimensions is an area of ongoing interest due to the broad scope of applications that could be addressed, including those in micro/nanomanufacturing, minimally invasive surgery, and sensing (12–15). Robots at these scales have the ability to perform tasks in spaces that would otherwise be difficult or impossible to access or across large scales in the environment or within biological systems in a distributed manner (16–18).

The structural complexity and material diversity of existing miniaturized robots are limited, currently constrained by options in manufacturing. As a result, at size scales in the submillimeter range, most robots take the form of simple spheres, tubes, rods, arcs, domes, or multilayer stacks of planar structures (19–22). Exceptions are in systems that adopt two-photon polymerization or stress-induced bending to yield 3D layouts (23–27). Recently reported submillimeter scale robots can perform multimodal locomotion in liquid media by mechanisms of light actuation (22, 28). On solid surfaces, however, light-actuated millimeter-scale robots cannot continuously move over a body length (29) or they require a rachet surface for directional locomotion (30).

Here, we introduce ideas that expand on these results to achieve submillimeter-scale robots in complex, 3D multimaterial designs with an unusual actuation scheme that enables motion on solid surfaces (Movie 1). The geometries span from arrays of curved filaments to complex folded architectures to biomimetic configurations, with

[1]Department of Biomedical Engineering, College of Future Technology, Peking University, Beijing 100871, China. [2]Institute of Advanced Structure Technology, Beijing Institute of Technology, Beijing 100081, China. [3]Applied Mechanics Laboratory, Department of Engineering Mechanics, Center for Flexible Electronics Technology, Tsinghua University, Beijing 100084, China. [4]National Key Laboratory of Nano/Micro Fabrication Technology, Institute of Microelectronics, Peking University, Beijing 100871, China. [5]Department of Electronic Engineering, The Chinese University of Hong Kong, New Territories, Hong Kong 999077, China. [6]Querrey Simpson Institute for Bioelectronics, Northwestern University, Evanston, IL 60208, USA. [7]Department of Aerospace and Mechanical Engineering, University of Southern California, Los Angeles, CA 90089, USA. [8]Department of Materials Science and Engineering, Northwestern University, Evanston, IL 60208, USA. [9]Key Laboratory of Specialty Fiber Optics and Optical Access Networks, Joint International Research Laboratory of Specialty Fiber Optics and Advanced Communication, Shanghai University, Shanghai 200444, China. [10]School of Materials Science and Engineering, University of Science and Technology Beijing, Beijing 100083, China. [11]Department of Mechanical Engineering, Johns Hopkins University, Baltimore, MD 21218, USA. [12]Department of Mechanical Engineering, Northwestern University, Evanston, IL 60208, USA. [13]School of Chemical Engineering and Technology, Tianjin University, Tianjin 300072, China. [14]Department of Materials Science and Engineering, Texas A&M University, College Station, TX 77843, USA. [15]Shanghai Frontiers Science Research Base of Intelligent Optoelectronics and Perception, Institute of Optoelectronics, Fudan University, Shanghai 200433, China. [16]State Key Laboratory of Functional Materials for Informatics, Shanghai Institute of Microsystem and Information Technology, Chinese Academy of Sciences, Shanghai 200050, China. [17]Department of Materials Science, Fudan University, Shanghai 200433, China. [18]Department of Civil and Environmental Engineering, Northwestern University, Evanston, IL 60208, USA. [19]Department of Biomedical Engineering, Northwestern University, Evanston, IL 60208, USA. [20]Department of Neurological Surgery, Northwestern University, Evanston, IL 60208, USA. [21]Department of Chemistry, Northwestern University, Evanston, IL 60208, USA. [22]Department of Electrical Engineering and Computer Science, Northwestern University, Evanston, IL 60208, USA.
*Corresponding author. Email: y-huang@northwestern.edu (Y.H.); yihuizhang@tsinghua.edu.cn (Y.Z.); jrogers@northwestern.edu (J.A.R.)
†These authors contributed equally to this work.
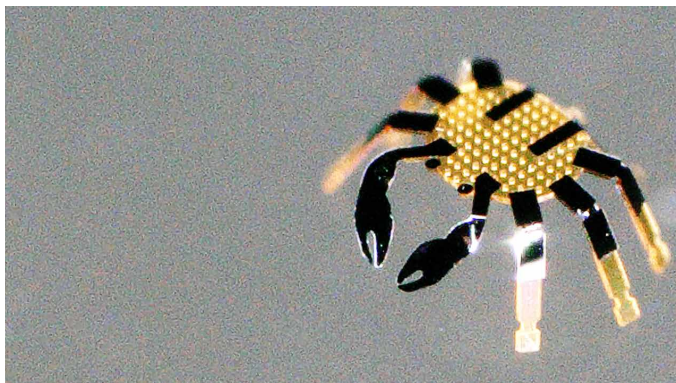
**Movie 1. Overview of the 3D submillimeter-scale robots.**

lateral dimensions down to ~200 µm and feature sizes to ~10 µm. These terrestrial robots consist of both organic and inorganic materials to support mechanical and optical forms of function. Programmed laser actuation of a shape memory alloy (SMA) integrated with a film coating that provides a restoring force enables various motion modalities, including but not limited to bending, twisting, crawling, and walking, with average speeds of up to ~0.44 body length/s, in systems with body lengths below 1 mm and weights of ~$10^{-5}$ g. Integrated photonic and sensing components support additional possibilities as a type of wireless communication and localization. These manufacturing approaches, actuation schemes, and design strategies are compatible with a wide range of materials, as the basis for a breadth of geometries, modalities, and functions that can be realized in small-scale robotic systems.

## RESULTS

### Fabrication and actuation of the robots

The complex 3D geometries of these submillimeter-scale robots originate from planar (2D) multilayer assemblies formed with deposition and patterning techniques used in the semiconductor industry. Figure 1 (A and B) illustrates the process of transformation that converts these 2D precursors into 3D shapes for the case of a design inspired by the geometry of a peekytoe crab (*Cancer irroratus*) but engineered to a much smaller dimensions (~1/150 of the actual size; fig. S1). The precursors incorporate layers of SMA (nitinol; 2.5 µm in thickness) as a collection of dynamic mechanical joints for locomotion, a film of polyimide (PI; ~8 µm in thickness) as a static skeleton for structural support, and pads of silicon dioxide (SiO$_2$; 100 nm in thickness) as bonding sites in the 2D to 3D transformation process (left frames in Fig. 1, A and B). This process begins with transfer printing to deliver these 2D precursors onto the surface of a prestretched silicone elastomer (Dragon Skin 10 Slow, ~500 µm in thickness) that supports structures of polydimethylsiloxane (PDMS; blocks) located near the claws and back legs (middle frame in Fig. 1B). Releasing the prestrain imposes compressive stresses at the bonding sites, with forces sufficient to convert the 2D structures into 3D architectures via a set of controlled bending/twisting deformations and translational/rotational motions (*31*, *32*). During this process, the distance between the two PDMS blocks also decreases, thereby deforming the claws and back legs. This transformation involves peak strains (<4%) that lie below the maximum phase transition strain of the SMA (right frame in Fig. 1B). Depositing an

additional conformal coating of SiO$_2$ (~1 µm in thickness) onto the resulting structures fixes their 3D shapes, thereby allowing for release as freestanding elements (right frame in Fig. 1A). The details appear in Materials and Methods, fig. S2, and Supplementary Methods. These processes convert micropatterned thin films of multiple materials with thicknesses between tens of nanometers and tens of micrometers into complex 3D geometries in a parallel fashion, uniquely enabling for unusual robots with millimeter and submillimeter scales. Related structures with centimeters or larger dimensions for robots that operate on similar principles can be realized using alternative techniques, such as laser engraving, mechanical cutting, and automatic robotic assembly.

This SiO$_2$ shell is a key component in the mechanism for reversible actuation, as illustrated by finite element analysis (FEA) in Fig. 1C. An increase in temperature transforms the SMA (nitinol) from the austenitic to the martensitic phase, causing the 3D structure to flatten into a 2D shape. The responses of the SMA elements at the joints act as driving forces to deform the PI skeleton. This process also elastically deforms the SiO$_2$ shell, resulting in a counter force that limits the magnitude of the deformation. The change in shape ceases when the forces from the shell balance those from the joints (right frame in Fig. 1C). Upon a reduction in temperature, the SMA changes from the martensitic back to the austenitic phase, thereby reducing the force produced by the SMA at the joints to zero. The elastic forces associated with the shell then push the entire system back to the original 3D geometry (left frame in Fig. 1C). Figure S3A simulates the moments generated by the SMA and the SiO$_2$ shell. In the FEA model, the SiO$_2$ shell appears on both the outer and inner surfaces of the 3D robot, consistent with experiments (fig. S3B). Although a single layer of the SiO$_2$ shell at the outer or inner surface can also provide restoring force, the double-layer shell structure follows naturally from the conformal deposition process. This actuation scheme allows for reversible shape transformations using a one-way shape memory material. Without the shell, the structure only supports a single change in shape, from 3D to 2D, as illustrated in fig. S3C. Figure 1D shows optical images of a freestanding 3D peekytoe crab on the edge of a coin, highlighting the preserved 3D geometry enabled by the SiO$_2$ shell after release from the elastomer substrate. Other 3D structures in geometries that resemble baskets, circular helices, and double-floor helices also exhibit high shape storage ratios (>85%) after cycles of heating and cooling (fig. S4). This ratio ($\varepsilon_s$) is defined as $\varepsilon_s = 1 - |L_1 - L_0|/L_0 \times 100\%$, where $L_0$ and $L_1$ are the distances between the bonding sites at both ends at the initial stage and subsequent stages, respectively.

This reversible actuation scheme offers stable performance in extended cycling tests (100,000 cycles), as validated using a simple 3D ribbon structure with one side bonded to a substrate (fig. S5), heated locally by exposure to a laser scanned at a frequency of 5 Hz for 7.5 hours. The laser used here has a spot size of 2.5 mm for easy alignment and a power of 188 mW (corresponding to an intensity of ~950 mW/cm$^2$) for effective heating. The irradiation conditions must be selected to avoid damage to the constituent materials (*33*). The experimental setup includes a microscope (Keyence, VHX-5000) to record the deformations (movie S1) and a customized algorithm to capture the position of the top edge (fig. S6). As shown in fig. S7, the mean and SD of the highest positions in the initial 50 cycles are 27.1 and 1.80 mm, respectively, and those after 135,000 cycles are 26.3 mm (mean of 50 cycles) and 2.19 mm (SD of 50 cycles). An indenter with fixed displacement serves as the basis for measurements
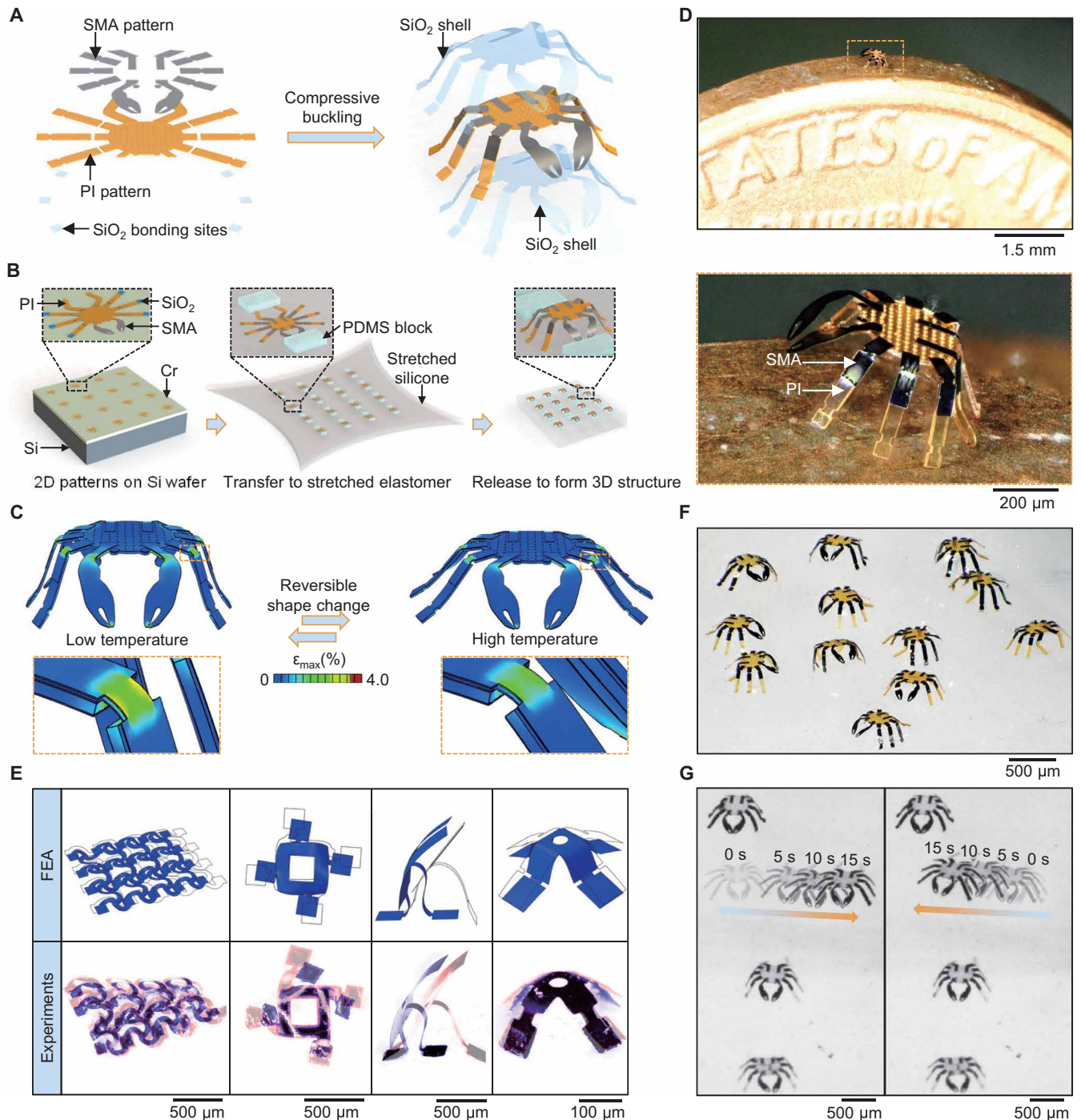
**Fig. 1. Wireless, reversible, and selective actuation of untethered, complex 3D mesostructures as submillimeter-scale terrestrial robots.** (**A**) Schematic exploded view illustration of a 3D robot in the shape of a peekytoe crab. Left: 2D multilayer precursor to this structure, with pads of SiO₂ to define bonding sites in a buckling process to yield the final 3D shape. Right: 3D mesostructure with a conformal coating of SiO₂ as an elastic encapsulating shell. (**B**) Schematic illustration of the fabrication process. (**C**) FEA results for a reversible actuation scheme that balances forces associated with phase transitions in an SMA with those that follow from the elastic resilience of the shell. (**D**) Optical images of a 3D peekytoe crab resting on the edge of a coin. (**E**) Superimposed images of various other 3D robotic structures. Top: FEA results, where images with blue color and black lines correspond to 3D geometries at room temperature and at ~100°C, respectively. Bottom: Experimental results; images colorized in blue and red correspond to 3D geometries at room temperature and at ~100°C, respectively. (**F**) Optical image of an array of 3D peekytoe crabs. (**G**) Selective actuation of one of the four crabs. Left: Directional locomotion from left to right. Right: Directional locomotion from right to left.

of forces generated from the 3D ribbon structure (fig. S8A). As shown in fig. S8B, the force reaches ~47 μN at 70°C.

The compatibility of the fabrication process with various thin-film deposition and etching techniques, laser patterning approaches, and photolithography methods creates broad possibilities in geometries and materials choices. Figure 1E, fig. S9, and movie S2 show examples of 3D robots with lateral dimensions ranging from ~200 μm to ~1.5 mm, with a diverse set of motion modalities, including bending, twisting, biaxial expansion, and combinations. For instance, the system in the second left frame of Fig. 1E exhibits both biaxial expansion (change in length $\Delta L/L_0 = $ ~0.15) and rotation (angle θ = ~2.1°) (fig. S10).

An important feature of the manufacturing procedures introduced here is that they operate in a parallel mode (that is, processing a large number of samples simultaneously), with the potential for mass production. Figure 1F demonstrates an array of freestanding 3D peekytoe crabs formed in a single set of processes on a common substrate, released, and then randomly distributed on a glass surface. Patterned laser exposure allows for selective activation. A simple

demonstration involves scanning a laser (wavelength: 520 nm; power: 188 mW; spot size: 2.5 mm) with a two-axis galvo to operate one of the crabs. Periodically (4 Hz in frequency) moving the laser spot from right to left across the body of the robot induces directional locomotion from left to right (left frame in Fig. 1G and movie S3), with an average speed of ~0.07 mm/s (fig. S11 and movie S4). Switching the direction of laser scanning reverses the motion, as shown in the right frame in Fig. 1G. The flexibility in choices of 3D geometry, constituent materials, and actuation modalities creates many opportunities for complex, multimodal means for locomotion and other forms of activation.

## Mechanism of directional locomotion

The mechanism of directional motion relies on an asynchronous change in shape during laser scanning. Detailed theoretical and experimental analyses of a simple 3D ribbon structure highlight the principles (Fig. 2). As illustrated in Fig. 2A, a laser moving from right to left induces sequential heating of the right, middle, and left parts of the 3D ribbon. The asymmetric shape of the 3D ribbon caused by
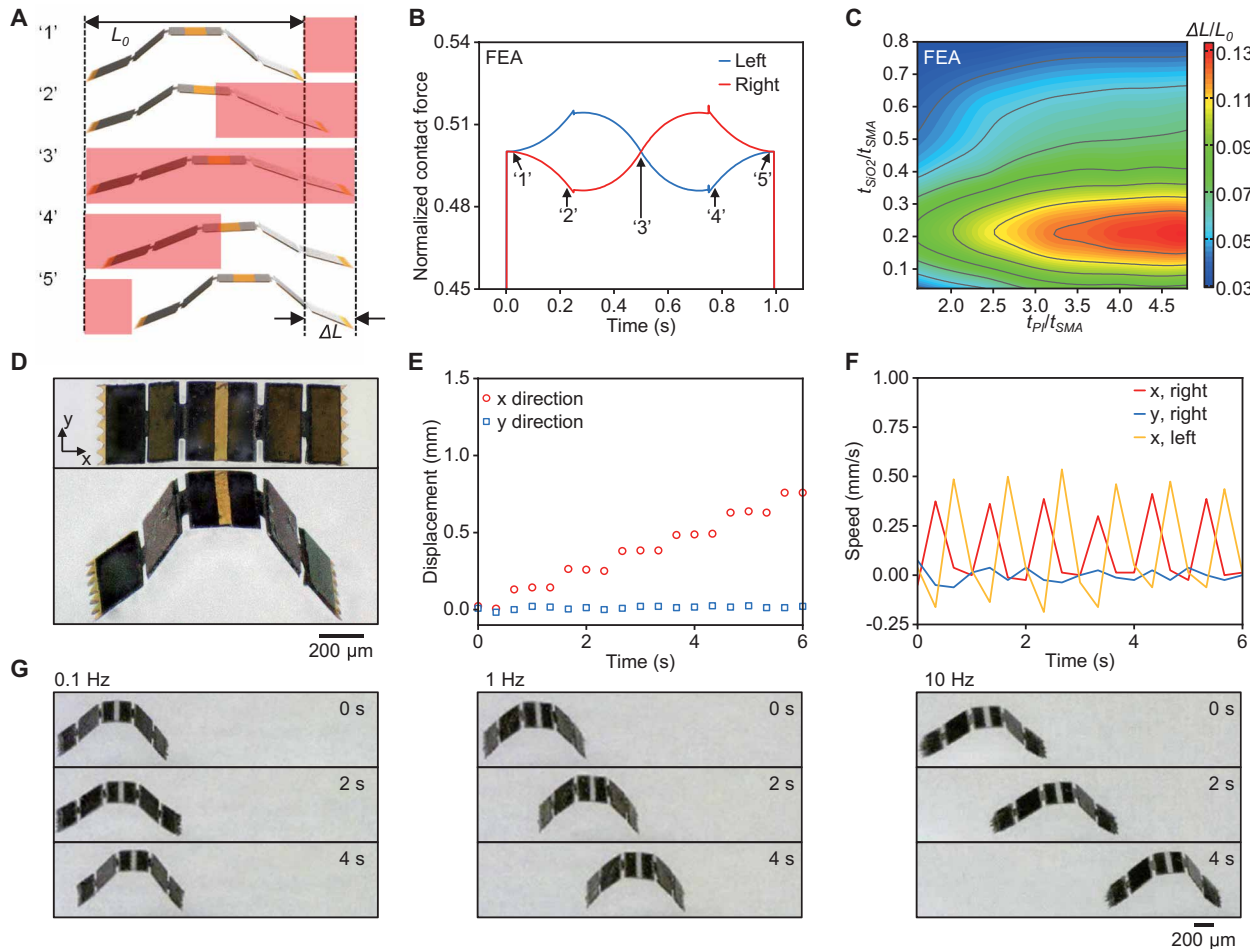


**Fig. 2. Mechanisms, optimization strategies, and characterization results for 3D submillimeter-scale terrestrial robots.** (**A**) Schematic illustration of sequential laser heating of a 3D ribbon structure that incorporates patterned features of SMA, PI, and SiO₂. The red background highlights regions with local heating. (**B**) Normalized contact forces of the left and right ends of the ribbon (from FEA). Circled numbers (1 to 5) correspond to the different states marked in (A). (**C**) $\Delta L/L_0$ of ribbons with different values of $t_{PI}/t_{SMA}$ and $t_{SiO2}/t_{SMA}$ computed by FEA ($t_{SMA} = 2.5$ μm for all cases). (**D**) Optical images (top frame: top view; bottom frame: tilted view) of the 3D ribbon. (**E** and **F**) Displacements (E) and speeds (left and right ends) (F) of motion along x and y axes at a laser scanning frequency of 1 Hz. (**G**) Locomotion for frequencies of 0.1, 1, and 10 Hz.

this time-dependent local heating leads to different normal forces at the points where the left and right sides of the ribbon contact the substrate (Fig. 2B). From state "1" to state "2," the right part of the 3D ribbon deforms due to a local increase in temperature. The normal contact force in this region decreases as a result. This force at the right end remains smaller than that at the left end, until the laser moves to the center of the ribbon (state "3"). In these cases, the right end of the ribbon moves to the right, while the left end of the structure remains static. As the laser scans to the left of the ribbon (states "4" and "5"), this part of the structure deforms, thereby reducing the associated normal contact force. The right end remains static due to the larger force, while the left end shrinks to the right as the temperature drops below the phase transition of the SMA.

This process of sequential local heating and associated asymmetric normal contact forces underpin directional locomotion. Similar concepts can also apply to robots with larger dimensions, as long as the deformations of different parts appear in a controlled order. An example is in a transparent soft robot that moves in a specific direction through programmed electrothermal heating of a metal nanowire network (34). Optimizing the geometric parameters enhances the normalized step length ($\Delta L/L_0$; illustrated in Fig. 2A) based on guidance from the results of FEA that considers fixed values for the body length ($L_0$) and the thickness of the SMA ($t_{SMA}$). Figure 2C depicts a contour plot of $\Delta L/L_0$ with respect to the normalized thicknesses of the PI skeleton ($t_{PI}/t_{SMA}$) and the SiO$_2$ shell ($t_{SiO2}/t_{SMA}$). The results indicate that $\Delta L/L_0$ increases with $t_{SiO2}/t_{SMA}$ until it reaches a maximum at a thickness ratio of ~0.25. Further increases in the thickness of the SiO$_2$ shell reduce the value of $\Delta L/L_0$ but improve the ability to maintain 3D shapes during actuation. By contrast, $\Delta L/L_0$ increases monotonically with $t_{PI}/t_{SMA}$, because thick layers of PI increase the strain energy that can be transferred to the SMA and SiO$_2$ at the crease regions that form as a consequence of the compressive buckling process.

Experimental demonstrations of the 3D ribbon robot appear in Fig. 2 (D to G). The ribbon has an initial length ($L_0$) of ~1 mm, with layers of SMA (2.5 μm in thickness), PI (~8 μm in thickness), and SiO$_2$ (~1 μm in thickness), as shown in Fig. 2D. Periodically scanning a continuous wave laser (wavelength: 520 nm; power: 188 mW; spot size: 2.5 mm; beam divergence: 1.5 mrad) over the structure from right to left induces a stepped, directional locomotion from left to right. Here, the 520-nm laser can effectively heat the SMA layer, as verified by the experimental results shown in figs. S12 and S13. Measurements of temperature exploits a planar submillimeter-scale SMA structure suspended in air by two PDMS supporting structures (fig. S14) to facilitate focusing of an infrared camera. The wavelength of 520 nm does not notably increase the temperature of the PI layer, consistent with its absorption spectrum (fig. S15). In comparison, lasers with shorter wavelengths (for example, <450 nm) substantially heat the PI to produce undesired expansion and deformation of the robot.

A set of optical images in fig. S16 shows the asynchronous deformation of the right and left parts of the ribbon, consistent with the analysis in Fig. 2 (A and B). A customized algorithm enables automatic detection of the edges and nodes of the 3D structures (fig. S17 and movie S5). The extracted coordinates at different time points facilitate further analysis of the dynamic behavior. Figure 2E shows the displacement of the 3D ribbon under a laser scanning frequency of 1 Hz. A stepped movement (average speed: ~0.12 mm/s) appears along the x axis (parallel to the laser scanning direction), whereas motions along the y axis (perpendicular to the laser scanning direction)

are negligible (average speed: ~0.001 mm/s; SD of position: 0.01 mm). As shown in Fig. 2F, the speeds of these ends reach local maxima successively with a time interval of ~0.33 s.

Adjusting the laser scanning frequency modulates the speed of movement. Reducing the frequency from 1 to 0.1 Hz reduces the average speed from ~0.12 to ~0.017 mm/s. The step length, $\Delta L$, for each cycle of movement ($\Delta L$, ~0.17 mm) at 0.1 Hz is larger than that at 1 Hz (~0.12 mm), due primarily to increased heating at low scanning frequencies (fig. S18). Increasing the frequency to 10 Hz yields an average speed of ~0.49 mm/s but with an $\Delta L$ of only 0.049 mm. Further increases of frequency lead to insufficient heating and reduced ability of the structure to deform and recover sufficiently, thereby decreasing the speed and, in the limit, preventing directional movement. Figure 2G and movie S6 show the 3D ribbon actuated at different frequencies (0.1, 1, and 10 Hz). A complete analysis of the displacement and speed of the 3D ribbon appears in fig. S19.

## Various structures and modes of locomotion

Elaborations in the structural designs and the laser scanning patterns yield diverse options in modes of locomotion. Figures S20 to S23 demonstrate 2D layouts and optical images of various robots made of SMA or combinations of SMA and PI. Detailed analyses of five representative 3D robots (shown in fig. S24, with extracted edges and nodes) provide insights into the broad variety of motions that are possible. The first example is a 3D ribbon of SMA and PI, as shown in Fig. 3A, figs. 25A and S26 (A to C), and movie S7. As before, local heating at different regions creates asymmetries in the geometries, as verified by FEA (left frame in Fig. 3A). Because of the asymmetric and asynchronous changes in shape, laser scanning from right to left leads to directional locomotion to the right; scanning from left to right reverses the direction. The middle frame of Fig. 3A shows superimposed images during a bidirectional linear crawling motion initiated using laser scanning at a frequency of 1 Hz. The average speed along the x axis (parallel to the laser scanning direction) reaches 0.11 mm/s (left to right) and −0.11 mm/s (right to left; right frame in Fig. 3A). These values are about five times larger than those along the y axis (perpendicular to the laser scanning direction, 0.021 and −0.027 mm/s).

Figure 3B shows a 3D robot that consists of two ribbons (different in length) connected together. After manual alignment of the laser to the robot, motion follows from automatic cyclic scanning of a line light source obtained by fast scanning of a point light source (wavelength: 520 nm; power: 188 mW; spot size: 2.5 mm; beam divergence: 1.5 mrad) via a sinusoidal input signal (20 Hz) to the y axis galvo that converts the point light source into a line (~5 mm in length) and a sawtooth wave (2 Hz) applied to the x axis galvo to move the line directionally from one side to the other along a linear trajectory (fig. S25B). When the laser irradiates the right part of the structure, both ribbons deform. In this case, the long ribbon exhibits a larger step (left frame in Fig. 3B) than the short ribbon. This difference results in a curvilinear trajectory. As the laser continues to scan from right to left, the robot moves to the right and rotates its body simultaneously, until the long side of the ribbon is perpendicular with the laser scanning direction (middle frame in Fig. 3B, figs. S27A and S28A, and movie S8). As the laser switches its scanning direction, the robot moves in a reversed direction in a curvilinear trajectory with a curvature radius of ~7 mm. Displacements, speeds, and trajectories appear in the right frame of Fig. 3B and fig. S26 (D to F).
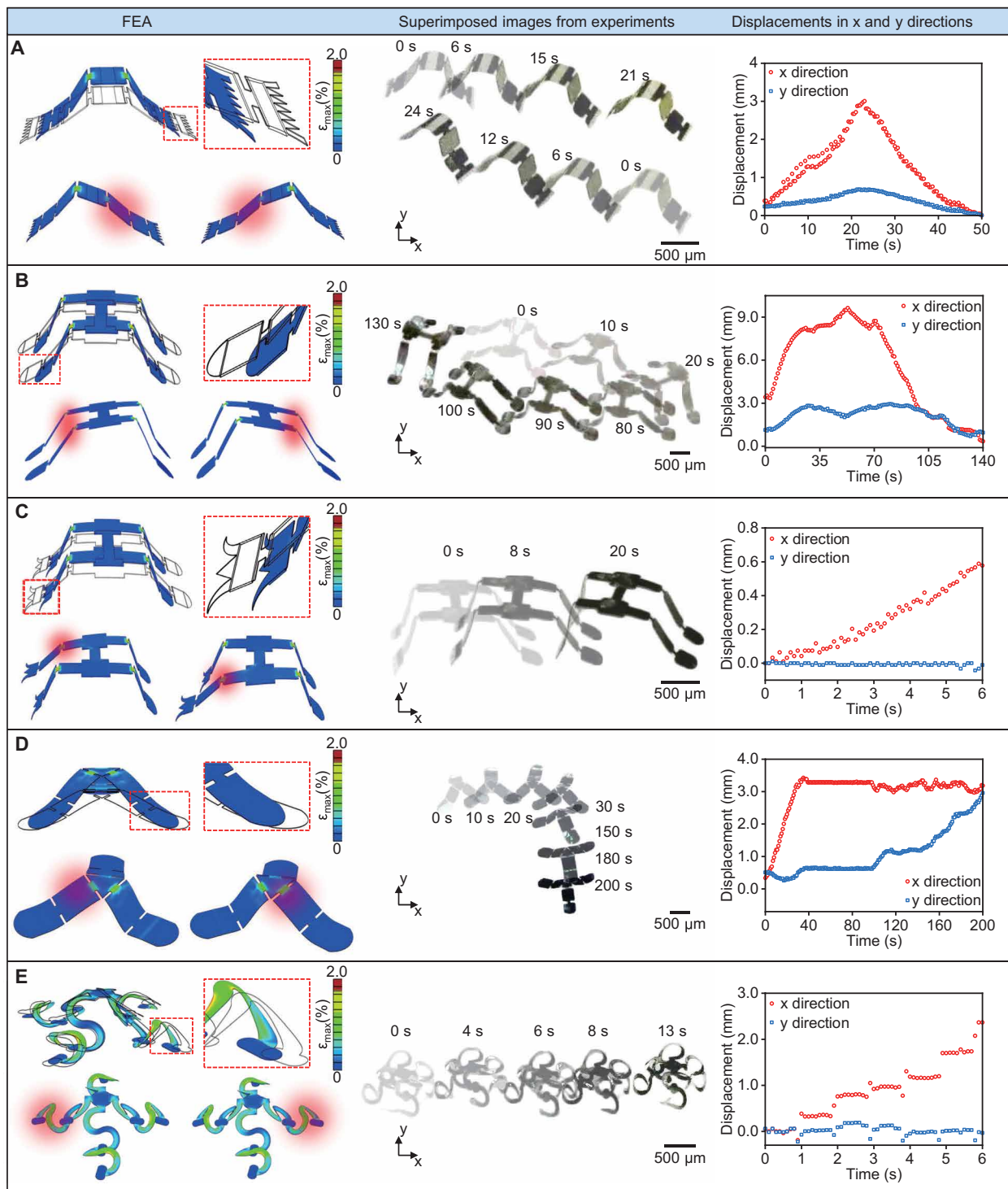
**Fig. 3. Various modes of locomotion enabled by 3D designs and schemes in sequential, local laser exposure.** (**A**) Bidirectional linear crawling motions of a 3D ribbon. (**B**) Bidirectional curvilinear crawling motions of a 3D robot with two interconnected asymmetric ribbons. (**C**) Walking motions realized through alternate heating of two ribbons. (**D**) Turning behaviors induced by changing the direction of laser scanning. (**E**) Jumping motions of a 3D robot with curvy legs. Left frames in (A) to (E) illustrate the FEA results of 3D robots under global heating (top; images with filled colors and black lines correspond to 3D geometries at room and elevated temperatures, respectively) and local heating (bottom; red dots indicate the positions of local heating). Middle frames in (A) to (E) present superimposed images of 3D robots. Right frames in (A) to (E) show displacements along the *x* and *y* directions at different time points.

Figure 3C presents a 3D robot that consists of two identical ribbons connected together. Tailored input signals to the galvo (fig. S25C) direct the laser (wavelength: 520 nm; power: 188 mW; spot size: 2.5 mm; beam divergence: 1.5 mrad) to alternatively heat the back sides of the two ribbons, causing sequential expansion (left frame in Fig. 3C). The result is a type of walking behavior, where two legs move forward by turns periodically, following the frequency of laser shifting (middle frame in Fig. 3C, figs. S27B and S28B, and movie S9). The average speed along the $x$ axis reaches ~0.11 mm/s for the case when the laser shifts between the two ribbons at a frequency of 3 Hz (right frame in Fig. 3C and fig. S26, G to I).

Other modes of locomotion involve turning (Fig. 3D) and jumping (Fig. 3E). The turning motion exploits a tri-legged 3D design. Laser heating causes deformations of any selected leg (left frame in Fig. 3D). This feature allows the robot to move along both the $x$ axis (laser scans from right to left at a frequency of 2 Hz) and $y$ axis (laser scans from bottom to top at a frequency of 2 Hz), as shown in the middle frame of Fig. 3D, figs. S27C and S28C, and movie S10. Average speeds along the $x$ and $y$ axes are 0.098 mm/s (from 0 to 35 s) and 0.030 mm/s (from 140 to 200 s), respectively (right frame in Fig. 3D and fig. S26, J to L). Figure 3E illustrates the jumping motion of a 3D robot induced by rapid changes in the shapes of curved ribbon structures (left and middle frames in Fig. 3E, figs. S27D and S28D, and movie S11). This behavior leads to a step change in the displacement curve, with a mean of 0.49 mm and an SD of 0.11 mm (right frame in Fig. 3E). The average speed along the $x$ axis is 0.42 mm/s for a frequency of 2 Hz. The instantaneous peak values of speed and acceleration in this jumping mode reach 5.7 mm/s and 81.9 mm/s$^2$, respectively (fig. S26, M to O), roughly five times larger than those in crawling, walking, and turning (fig. S26). These light-actuated

robots can also perform locomotion on the surface of water. Figure S29 and movie S12 show a tri-legged robot operating in this manner under laser scanning at 1 Hz. Capabilities for operation under the water are limited by effects in surface tension and heat dissipation (fig. S30). In this sense, application opportunities for robots with the designs reported here complement those in biomedicine and other areas where alternative approaches are preferred. In all of these cases, the wavelength, power, and spot size of the laser are 520 nm, 188 mW, and 2.5 mm, respectively.

Figure 4 compares the dimensions and speeds of various robots actuated through light exposure, magnetic fields, battery power, and chemical reactions. Table S1 summarizes the key parameters, including speed, body length, actuation mechanism, operation environment, complexity of geometry, and others. Compared with other robots that adopt complex 3D geometries and multimaterial construction (Fig. 4, references with underlines and ellipse with brown shading), the robots demonstrated here have the smallest dimensions (~750 μm; 3D structures that resemble peekytoe crabs). Among light-actuated robots (yellow symbols in Fig. 4), ours can operate at relatively fast speeds (~0.44 body length/s). This fast movement behavior follows from submillimeter dimensions that accelerate heat dissipation (fig. S31), advanced 3D designs that optimize motions, and actuation schemes that enable reversible deformations at high strain and stress using a one-way SMA (35, 36). Further reductions in the dimensions increase the rates of heat dissipation and, theoretically, the speed per body length, as verified by FEA in fig. S32. This analysis only incorporates, however, the actuation forces from the SMA and the friction forces with the substrate, without considering other types of forces that may exist in practical scenarios (for example, electrostatic adhesion and van der Waals force) or various perturbations associated with the environment (for example, air flow). The summation of these forces together with the static friction, both of which increase substantially with reductions in size, could fundamentally limit the operation, depending on the detailed circumstances.

Two ellipses with red and blue dashed lines in Fig. 4 separate robots that operate in terrestrial and aquatic environments. The body lengths of aquatic robots span from the micrometer to centimeter scale. For terrestrial operation, microscale robots move on special surfaces that present ratchet structures (30) or interdigital electrodes (27), or they cannot move continuously over a body length (29). Previously reported terrestrial robots that can continuously operate on unstructured surfaces have dimensions in the millimeter to centimeter range. The manufacturing approaches, actuation schemes, and structural design approaches introduced here allow for body lengths (~0.75 mm) that are more than three times smaller than those of the smallest terrestrial robots reported previously (2.5 mm in body length) (37).
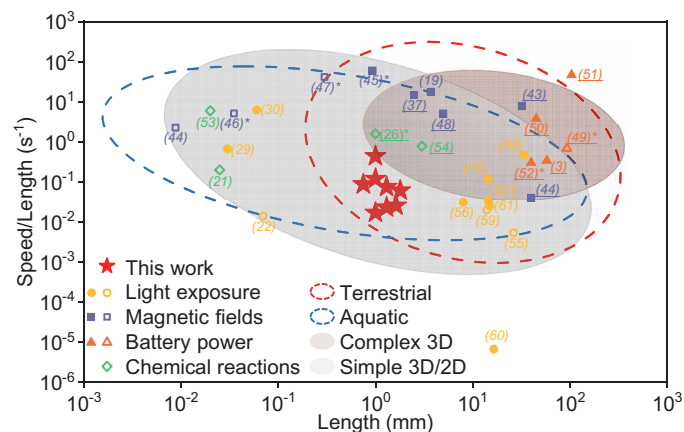


**Fig. 4. Summary of reported robots plotted as the ratio of maximum speed to body length as a function of length.** The plot includes robots that operate in terrestrial and aquatic environments through actuation based on light exposure, magnetic fields, battery power, and external chemical reactions. Solid symbols and the region bounded by the red dashed ellipse (68% confidence interval) correspond to terrestrial robots. Hollow symbols and the region bounded by the blue dashed ellipse (68% confidence interval) correspond to aquatic robots. Details of the references appear in table S1. References with underlines and the brown shaded ellipse (68% confidence interval) correspond to robots with complex 3D geometries. References without underlines and the gray shaded ellipse (68% confidence interval) correspond to robots without complex 3D geometries. References marked with "*" correspond to robots that can change directionality during movement in a controllable way.

## Applications in telemetry and localization
Capabilities in telemetry and localization are also essential for these types of systems (13). An optical approach is useful to consider in the context of light-actuated robots such as those presented here. Photonic elements, colorimetric reagents, and retroreflectors can support basic forms of telemetry. Figure 5A shows a setup that includes a shutter and a two-axis galvo to modulate and control the position of two laser beams at different wavelengths (445 and 638 nm). A retroreflector integrated on the robot allows light to reflect back to the beam splitter along the direction of incidence. The retroreflector used here exploits a corner cube geometry design (Fig. 5B and
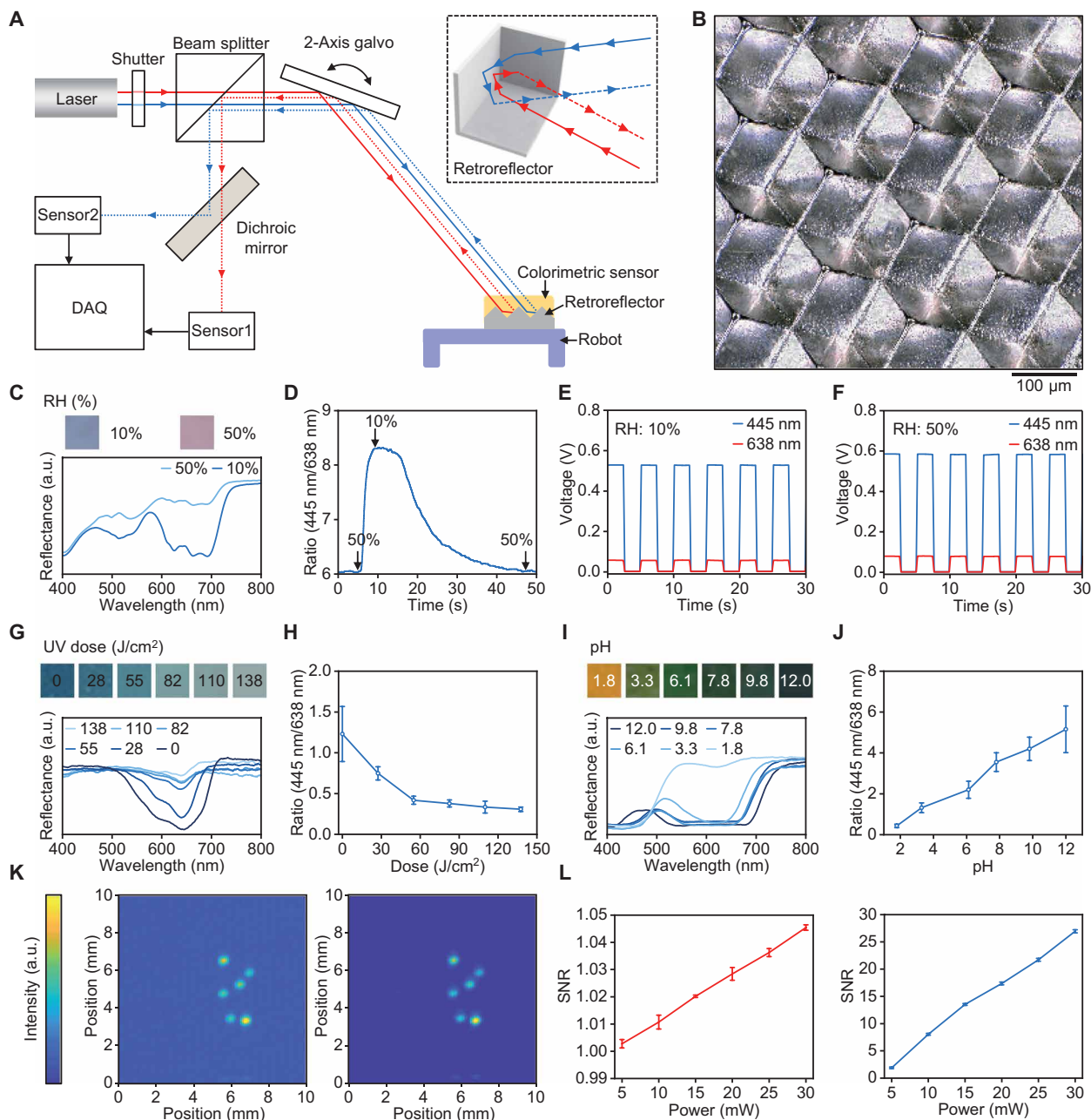
**Fig. 5. Telemetry and localization achieved by integrating retroreflectors and colorimetric sensing materials into 3D robots.** (**A**) Schematic illustration of the optical setup for telemetry. Inset: Schematic illustration of one unit of the corner cube retroreflector. (**B**) Optical image of the retroreflector. (**C**) Optical images (top) and reflectance (bottom) of a colorimetric humidity sensor exposed to dry [relative humidity (RH): ~10%] and humid (RH: ~50%) air. (**D**) Ratio between the voltages of the photodetectors for blue and red lasers as the RH changes from ~50 to ~10%. (**E** and **F**) Time-domain output voltages of photodetectors for the blue and red laser light, measured at a RH of ~10% (E) and ~50% (F). A shutter modulates the laser exposure at a frequency of 0.2 Hz. (**G** and **H**) Optical images [top frame in (G)], reflectance [bottom frame in (G)], and ratio between the voltages of the photodetectors for the blue and red laser light (H) for the colorimetric UV sensor under different doses of UV exposure. (**I** and **J**) Optical images [top frame in (I)], reflectance [bottom frame in (I)], and ratio between the voltages of the photodetectors for the blue and red laser light (J) for the colorimetric pH sensor after immersion in solutions with different pH. (**K**) Example of localizing six robots through laser scanning in bright (left) and dark (right) environments. (**L**) Plot of SNR as a function of input power in bright (left) and dark (right) environments. Error bars are SE deviations from 10 cycles ($N = 10$) of measurements. a.u., arbitrary units.

figs. S33 and S34), with a side length of 100 µm, fabricated through two-photon lithography, a multiple demolding process, and conformal deposition of silver (details appear in Materials and Methods). A semitransparent colorimetric material placed on top of the reflector absorbs a portion of the light, thereby affecting the intensities of the reflected light. The setup directs light from two lasers onto the retroreflector and separates the reflected light through a dichroic mirror (long-pass, cut-on wavelength: 567 nm). Two photodetectors detect

the reflected light in the form of voltage signals associated with the intensities. The ratio of these voltages can determine the absorbance of the colorimetric material in a way that mitigates the influence of other factors, such as changes in distance or optical properties of the surroundings (*38*).

Colorimetric materials can be used in this manner for remote sensing of different species or parameters associated with the surroundings. For example, the color of a mixture of $CoCl_2$ and silicone elastomer (Ecoflex 00-30) changes from blue to pink as the humidity increases from ~10 to ~50%. Figure 5C shows the reflectance of such a mixture coated onto the retroreflector, across a wavelength range from 400 to 800 nm. At low humidity, the reflectance at 445 nm remains largely unchanged, but the reflectance at 638 nm shows notable decrease. Figure 5D shows the ratio of the voltages from the two photodetectors (445 and 638 nm) as the humidity decreases from ~50 to ~10%. As in Fig. 5 (E and F), voltages associated with the 445- and 638-nm light exhibit stable values during cyclic measurements performed using a shutter to modulate the laser exposures. Additional results appear in fig. S35.

Colorimetric materials that respond to pH and ultraviolet (UV) light offer additional capabilities in sensing. The latter uses a composite of UV-bleachable dye (CR234-BT2B, Spectra Group Inc.) in PDMS (10:1; Sylgard 184) to form a semitransparent gel that changes from dark blue to light gray upon UV exposure. Figure 5G shows the reflectance of a sensor formed by coating this material on the retroreflector for different doses of UV exposure. A high UV dose decreases the reflectance at 638 nm and increases the reflectance at 445 nm. The ratio of the voltages from the two photodetectors exhibits a monotonic relationship with UV dose, as shown in Fig. 5H. The pH-sensitive material (details appear in Materials and Methods) changes in color from yellow (pH = 1.8) to green (pH = 6.1) and to dark blue (pH = 12.0; Fig. 5I) with increasing pH. Consequently, the voltage ratio increases monotonically with pH (Fig. 5J). Additional results appear in fig. S36.

The setup in Fig. 5A also enables the localization of these robots with a single laser beam. Applying a cyclic step signal (duration: 0.01 s; step height: 0.02 V; number of steps: 100) to the *x* axis galvo and a sawtooth signal (maximum voltage: 1 V; minimum voltage: −1 V; frequency: 100 Hz) to the *y* axis galvo scans the laser across a 2D surface (fig. S37). The voltage generated from the photodetector reaches a maximum when the laser beam illuminates the retroreflector and reflects it in the direction of incidence. Tracking the intensity of this reflected light (that is, voltages generated from photodetectors) provides a means for localization. As shown in Fig. 5K, laser scanning across a 1 cm–by–1 cm area yields six spots with high intensities, corresponding to the positions of six robots. The power of the laser and the ambient light influence the signal-to-noise ratio (SNR). Figure 5L and fig. S38 compare the SNRs, spatial intensity maps, and time-domain voltage signals from the photodetector for both bright and dark environments for laser powers between 5 and 30 mW. In a bright environment, a laser power of 5 mW is sufficient to distinguish the positions of the robots (SNR: ~1.003). Incorporating narrow bandpass filters, using lasers with small spot sizes, and applying multiple cycles of laser scanning are effective means to improve the performance of this simple scheme.

These capabilities in telemetry and localization allow the robots to serve as distributed and mobile sensors in the environment, limited spaces, or biological systems. For this last possibility, light delivery might involve implanted optical fibers, instrumented catheters, or microscale light sources, preferably operating in the infrared to minimize absorption by tissues. One potential application is in photothermal therapy, where robots coated with gold nanorods could be actuated through irradiation with infrared light once in the position of interest.

## DISCUSSION

The results presented here provide effective means to construct submillimeter-scale robots with heterogeneous material construction and complex 3D structures. The manufacturing approach can combine multilayer, lithographically defined structures of organic and inorganic materials together in systems that adopt complex 3D geometries. Thermal actuation of SMA within an elastic framework enables reversible deformations of the robots. Laser-induced sequential heating modulates the normal contact forces at different parts of the robot to enable directional terrestrial locomotion—including linear/curvilinear crawling, walking, turning, and jumping—with average speeds up to ~0.44 body length/s. Photonic components and colorimetric sensors integrated onto the bodies of these robots provide means for wireless communication and localization.

These multimaterial terrestrial robots at submillimeter-scale sizes incorporate improvements in actuators, advanced materials, bioinspired designs, fabrication methods, and sensors. The strategy in constructing untethered 3D robots represents a general approach that can apply to other mechanically responsive materials as well. Specifically, the robots presented here have three key features that promote the performance and expand the functions of small-scale systems. First, the submillimeter dimensions lead to high rates of heat dissipation and, thus, fast moving speeds on unstructured, solid surfaces. Second, the diversity of 3D geometries and laser scanning patterns broadens the motion modalities. Third, the combination of mechanically and optically functional materials enables capabilities in telemetry and localization. These advances can expand the range of materials, geometries, modalities, and functions of small-scale robotic systems and facilitate practical applications in monitoring the structural health of machines, modulating various biological processes in lab-on-a-chip systems, and enabling minimally invasive surgical procedures and others.

## MATERIALS AND METHODS
### Fabrication of 3D submillimeter-scale robots using SMA and single layers of PI

The procedure began with annealing samples (Si/Cr/SMA, 500 μm/ 50 nm/2.5 μm in thickness) at 500°C in vacuum for 30 min. Photolithography and wet etching ($HNO_3$:HF:$H_2O$ = 1:1:10) formed patterns in the SMA. Spin coating PI (PI2545, ~8 μm in thickness) and depositing Cu by electron beam evaporation (100 nm in thickness) formed additional coatings on top of the SMA. Wet etching of Cu and dry etching [March reactive ion etching (RIE)] of PI defined the geometry of the PI skeleton. Undercut etching of the Cr facilitated transfer of the resulting 2D precursors in SMA and PI to a water-soluble tape. Deposition of $SiO_2$ (100 nm in thickness) through a shadow mask formed the bonding sites. A compressive buckling process (*39–41*) transformed the 2D precursors into 3D robots tethered to a silicone elastomer substrate. Conformal coating $SiO_2$ (1 μm in thickness) via sputter deposition fixed the 3D geometries. Dissolving the silicone substrate in a commercial mixture of solvents (Dynasolve)

while sonicating yielded freestanding, untethered 3D robots. Additional details appear in Supplementary Methods.

## Fabrication of 3D submillimeter-scale robots in SMA and double layers of PI

The process began with annealing samples (Si/Cr/SMA, 500 μm/ 50 nm/2.5 μm in thickness) at 500°C in vacuum for 30 min. Photolithography and wet etching with a mixture of $HNO_3$ and HF defined patterns in the SMA. After spin coating PI (PI2545, 3 to 8 μm in thickness) and depositing Cr/Au (10 nm/100 nm in thickness), photolithography and wet etching defined a hard mask in the Cr/ Au for subsequent dry etching of PI. Peeling the PI layer from the Si substrate released the SMA pattern and the Cr layer underneath. Removing the exposed Cr and photoresist yielded a flexible film of PI with a pattern of SMA. Next, transfer of the flexible film onto a PDMS-coated glass with SMA pattern facing up prepared the substrate for another coating of PI layer. Oxygen plasma etching (March RIE) of PI with Au pattern facing up defined a pattern in the PI. Removing the Au and Cr completed the fabrication of the 2D precursors. Transferring the 2D precursors to a water-soluble tape and depositing $SiO_2$ through a shadow mask created the bonding sites. Subsequent steps followed those mentioned above. Additional details appear in Supplementary Methods.

## Fabrication of 3D submillimeter-scale robots in SMA

The process began with annealing samples (Si/Cr/SMA, 500 μm/ 50 nm/2.5 μm in thickness) at 500°C in vacuum for 30 min. Photolithography and wet etching with a mixture of $HNO_3$ and HF defined patterns in the SMA. After undercut etching the Cr, transferring the 2D precursors to a water-soluble tape and depositing $SiO_2$ through a shadow mask created the bonding sites. Subsequent steps followed those mentioned above. Additional details appear in Supplementary Methods.

## Fabrication and integration of corner cube retroreflectors

A 3D printing system (Nanoscribe) formed the corner cube structure (100 μm in side length) in photodefinable epoxy. Casting a mixture of PDMS (10:1; Sylgard 184) on the epoxy mold and separating the two materials formed an inversed mold in PDMS. Dip coating a layer of a precursor to PI (PI2545) on the mold, pressing the uncured PI with a glass slide, and heating at 110°C for 2 hours produced a corner cube structure in PI. Sputter depositing Ti/Ag (10 nm/100 nm in thickness) on the PI structure increased the reflectance and completed the fabrication of the corner cube retroreflector. After manually cutting the Ag-coated PI structures into small pieces, the bottom surface of each small piece was dipped to a layer of uncured PDMS and manually aligned to the robot under microscope.

## Optical setup for controlling the submillimeter-scale robots

The optical setup for controlling the locomotion of the 3D robots included a laser (LSR-RGB-1W-FC, Civil Laser), a customized two-axis galvo, and a digital microscope (VHX-5000, Keyence). The two-axis galvo allowed programmable laser scanning on a plate under the field of view of the microscope. Imaging through the microscope yielded videos at a rate of 30 frames/s and with adjustable tilt angles from 0° to 90°.

## Optical setup for telemetry

The setup for telemetry included a laser (LSR-RGB-1W-FC, Civil Laser), a shutter (SHB025, Thorlabs), a beam splitter (CCM1-BS013, Thorlabs), a customized two-axis galvo, a dichroic mirror (DMLP567, Thorlabs), photodetectors (SG88MQ-415, Shine Gold Electronics), transimpedance amplifiers (ADA4505-2), and a PowerLab system (Model 8/35, ADInstruments). Red (638 nm) and blue (445 nm) laser beams passed through the shutter and beam splitter, controlled by the two-axis galvo to irradiate colorimetric materials coated on the retroreflector. A dichroic mirror passed the red light and reflected the blue light. Two photodetectors produced current signals, recorded as voltages in the PowerLab system after passing through two transimpedance amplifiers at a sampling rate of 200 k/s.

## Optical setup for localization

Localization exploited setups similar to those for telemetry but without the dichroic mirror and with only one photodetector and transimpedance amplifier. The two-axis galvo allowed raster scanning of the laser beam over a predefined area. Customized MATLAB code decoded the time-domain signal to yield an intensity map as a means for localization.

## Stability test

A 3D ribbon robot, with one side fixed onto a rigid metal plate, served as the structure for mechanical characterization (fig. S5). Laser irradiation at a frequency of 7.5 Hz and a power of 188 mW periodically heated the robot. A digital microscope (VHX-5000, Keyence) recorded the resulting motions at a rate of 30 frames/s. A customized Python code detected the positions of the top surface in each frame.

## Preparation of colorimetric materials for pH sensing

Tetrahydrofuran served as the solvent to dissolve bromothymol blue [1.5 weight % (wt %)], polyvinyl chloride (27.4 wt %; average molecular weight: ~233,000), and trioctylmethylammonium chloride (5.1 wt %; Aliquat 336). Stirring at room temperature for ~5 hours created a homogeneous mixture. Adding o-nitrophenyloctylether (66.0 wt %) to the mixture created a colorimetric material for sensing pH. Spin casting (1500 rpm) on a retroreflector and drying at room temperature for ~20 min formed the pH-sensitive layer. Hydrochloric acid and aqueous solutions of sodium hydroxide with different concentrations changed the color of the pH-sensitive colorimetric material. The color of the material changed from orange to yellow in acidic solution and to blue in alkaline solution after fully dried.

## Preparation of colorimetric materials for UV sensing

A mixture of the UV-bleachable dye (CR234-BT2B, Spectra Group Inc.) and PDMS (10:1; Sylgard 184) at a weight ratio of 1:20 served as a colorimetric material for sensing UV irradiation. Degassing under vacuum for 1 hour removed bubbles in the mixture. Spin casting (1500 rpm) followed by curing at room temperature created a uniform UV-sensitive layer on the retroreflector. The color of the material changed from blue to semitransparent under UV irradiation.

## Preparation of colorimetric materials for humidity sensing

The colorimetric material for sensing humidity consisted of a mixture of $CoCl_2$ and silicone elastomer (Ecoflex 00-30) at a weight ratio of 1:20. Spin casting (1000 rpm) and curing at room temperature for 1 hour formed a humidity-sensitive layer on the retroreflector. The material exhibited a blue color in dry air and a pink color in humid air.

## Finite element analysis

Simulations of the shape transformation of 2D precursors to 3D structures and mechanical responses of 3D structures upon increases in temperature used the commercial software ABAQUS

(Supplementary Methods). Eight-node 3D solid elements and four-node shell elements were used for modeling the substrate and multilayered film, respectively. Refined meshes were adopted to ensure computational accuracy. First, linear buckling analyses were performed to determine the critical buckling strain for the filamentary ribbons, which were then implemented as initial geometric imperfections in the post-buckling simulation. The elastic modulus $E$ and Poisson's ratio $\nu$ were $E_{PI} = 3$ GPa and $\nu_{PI} = 0.34$ for PI, $E_{PDMS} = 166$ kPa and $\nu_{PDMS} = 0.49$ for PDMS, and $E_{SiO2} = 66$ GPa and $\nu_{SiO2} = 0.27$ for $SiO_2$. The elastic moduli for the austenitic and martensitic phases of NiTi SMA were 80 and 30 GPa, respectively. The starting temperature (the temperature that triggers the phase transition of the SMA) and the finishing temperature (the temperature above which the phase transition ceases) were 40° and 75°C, respectively (fig. S18). Simulations of the motions only considered the temperature change between the starting and finishing temperatures. The heat flux, environmental temperature, and convective heat transfer coefficient were 0.5 mW/mm$^2$, 25°C, and 8 W/(m$^2\cdot$K), respectively.

## Statistical analysis

Data are presented as single values. This paper investigates the performances of a proof-of-concept submillimeter-scale robot, and statistical analysis was not performed except for the results of telemetry and localization (Fig. 5, H, J, and L). Data points and error bars are mean values and SE deviations from 10 cycles ($N = 10$) of measurements, respectively. Curves drawn on top of data directly connect the data points without fitting.

## SUPPLEMENTARY MATERIALS

## REFERENCES AND NOTES

1. K. Y. Ma, P. Chirarattananon, S. B. Fuller, R. J. Wood, Controlled flight of a biologically inspired, insect-scale robot. *Science* **340**, 603–607 (2013).
2. E. Chang, L. Y. Matloff, A. K. Stowers, D. Lentink, Soft biohybrid morphing wings with feathers underactuated by wrist and finger motion. *Sci. Robot.* **5**, eaay1246 (2020).
3. Z. Zhakypov, K. Mori, K. Hosoda, J. Paik, Designing minimal and scalable insect-inspired multi-locomotion millirobots. *Nature* **571**, 381–386 (2019).
4. D. Rus, M. T. Tolley, Design, fabrication and control of soft robots. *Nature* **521**, 467–475 (2015).
5. S.-J. Park, M. Gazzola, K. S. Park, S. Park, V. D. Santo, E. L. Blevins, J. U. Lind, P. H. Campbell, S. Dauth, A. K. Capulli, F. S. Pasqualini, S. Ahn, A. Cho, H. Yuan, B. M. Maoz, R. Vijaykumar, J.-W. Choi, K. Deisseroth, G. V. Lauder, L. Mahadevan, K. K. Parker, Phototactic guidance of a tissue-engineered soft-robotic ray. *Science* **353**, 158–162 (2016).
6. S. Hashemi, D. Bentivegna, W. Durfee, Bone-inspired bending soft robot. *Soft Robot.* **8**, 387–396 (2021).
7. E. W. Hawkes, L. H. Blumenschein, J. D. Greer, A. M. Okamura, A soft robot that navigates its environment through growth. *Sci. Robot.* **2**, eaan3028 (2017).
8. Y. Wang, X. Yang, Y. Chen, D. K. Wainwright, C. P. Kenaley, Z. Gong, Z. Liu, H. Liu, J. Guan, T. Wang, J. C. Weaver, R. J. Wood, L. Wen, A biorobotic adhesive disc for underwater hitchhiking inspired by the remora suckerfish. *Sci. Robot.* **2**, eaan8072 (2017).
9. C. Larson, B. Peele, S. Li, S. Robinson, M. Totaro, L. Beccai, B. Mazzolai, R. Shepherd, Highly stretchable electroluminescent skin for optical signaling and tactile sensing. *Science* **351**, 1071–1074 (2016).
10. N. T. Jafferis, E. F. Helbling, M. Karpelson, R. J. Wood, Untethered flight of an insect-sized flapping-wing microscale aerial vehicle. *Nature* **570**, 491–495 (2019).
11. G. Li, X. Chen, F. Zhou, Y. Liang, Y. Xiao, X. Cao, Z. Zhang, M. Zhang, B. Wu, S. Yin, Y. Xu, H. Fan, Z. Chen, W. Song, W. Yang, B. Pan, J. Hou, W. Zou, S. He, X. Yang, G. Mao, Z. Jia,

H. Zhou, T. Li, S. Qu, Z. Xu, Z. Huang, Y. Luo, T. Xie, J. Gu, S. Zhu, W. Yang, Self-powered soft robot in the Mariana Trench. *Nature* **591**, 66–71 (2021).
12. Q. Liu, W. Wang, M. F. Reynolds, M. C. Cao, M. Z. Miskin, T. A. Arias, D. A. Muller, P. L. McEuen, I. Cohen, Micrometer-sized electrically programmable shape-memory actuators for low-power microrobotics. *Sci. Robot.* **6**, eabe6663 (2021).
13. B. J. Nelson, I. K. Kaliakatsos, J. J. Abbott, Microrobots for minimally invasive medicine. *Annu. Rev. Biomed. Eng.* **12**, 55–85 (2010).
14. M. Sitti, H. Ceylan, W. Hu, J. Giltinan, M. Turan, S. Yim, E. Diller, Biomedical applications of untethered mobile milli/microrobots. *Proc. IEEE* **103**, 205–224 (2015).
15. A. Ghosh, W. Xu, N. Gupta, D. H. Gracias, Active matter therapeutics. *Nano Today* **31**, 100836 (2020).
16. V. B. Koman, P. Liu, D. Kozawa, A. T. Liu, A. L. Cottrill, Y. Son, J. A. Lebron, M. S. Strano, Colloidal nanoelectronic state machines based on 2D materials for aerosolizable electronics. *Nat. Nanotechnol.* **13**, 819–827 (2018).
17. B. H. Kim, K. Li, J.-T. Kim, Y. Park, H. Jang, X. Wang, Z. Xie, S. M. Won, H.-J. Yoon, G. Lee, W. J. Jang, K. H. Lee, T. S. Chung, Y. H. Jung, S. Y. Heo, Y. Lee, J. Kim, T. Cai, Y. Kim, P. Prasopsukh, Y. Yu, X. Yu, R. Avila, H. Luan, H. Song, F. Zhu, Y. Zhao, L. Chen, S. H. Han, J. Kim, S. J. Oh, H. Lee, C. H. Lee, Y. Huang, L. P. Chamorro, Y. Zhang, J. A. Rogers, Three-dimensional electronic microfliers inspired by wind-dispersed seeds. *Nature* **597**, 503–510 (2021).
18. Y. Kim, G. A. Parada, S. Liu, X. Zhao, Ferromagnetic soft continuum robots. *Sci. Robot.* **4**, eaax7329 (2019).
19. W. Hu, G. Z. Lum, M. Mastrangeli, M. Sitti, Small-scale soft-bodied robot with multimodal locomotion. *Nature* **554**, 81–85 (2018).
20. J. Mu, C. Hou, H. Wang, Y. Li, Q. Zhang, M. Zhu, Origami-inspired active graphene-based paper for programmable instant self-folding walking devices. *Sci. Adv.* **1**, e1500533 (2015).
21. Z. Wu, L. Li, Y. Yang, P. Hu, Y. Li, S.-Y. Yang, L. V. Wang, W. Gao, A microrobotic system guided by photoacoustic computed tomography for targeted navigation in intestines in vivo. *Sci. Robot.* **4**, eaax0613 (2019).
22. M. Z. Miskin, A. J. Cortese, K. Dorsey, E. P. Esposito, M. F. Reynolds, Q. Liu, M. Cao, D. A. Muller, P. L. McEuen, I. Cohen, Electronically integrated, mass-manufactured, microscopic robots. *Nature* **584**, 557–561 (2020).
23. C. C. J. Alcântara, S. Kim, S. Lee, B. Jang, P. Thakolkaran, J.-Y. Kim, H. Choi, B. J. Nelson, S. Pané, 3D fabrication of fully iron magnetic microrobots. *Small* **15**, 1805006 (2019).
24. Z. Tian, B. Xu, B. Hsu, L. Stan, Z. Yang, Y. F. Mei, Reconfigurable vanadium dioxide nanomembranes and microtubes with controllable phase transition temperatures. *Nano Lett.* **18**, 3017–3023 (2018).
25. Q. Jin, Y. Yang, J. A. Jackson, C. Yoon, D. H. Gracias, Untethered single cell grippers for active biopsy. *Nano Lett.* **20**, 5383–5390 (2020).
26. V. K. Bandari, Y. Nan, D. Karnaushenko, Y. Hong, B. Sun, F. Striggow, D. D. Karnaushenko, C. Becker, M. Faghih, M. Medina-Sánchez, F. Zhu, O. G. Schmidt, A flexible microsystem capable of controlled motion and actuation by wireless power transfer. *Nat. Electron.* **3**, 172–180 (2020).
27. B. R. Donald, C. G. Levey, C. D. McGray, I. Paprotny, D. Rus, An untethered, electrostatic, globally controllable MEMS micro-robot. *J. Microelectromech. Syst.* **15**, 1–15 (2006).
28. S. Palagi, A. G. Mark, S. Y. Reigh, K. Melde, T. Qiu, H. Zeng, C. Parmeggiani, D. Martella, A. Sanchez-Castillo, N. Kapernaum, F. Giesselmann, D. S. Wiersma, E. Lauga, P. Fischer, Structured light enables biomimetic swimming and versatile locomotion of photoresponsive soft microrobots. *Nat. Mater.* **15**, 647–653 (2016).
29. O. J. Sul, M. R. Falvo, R. M. Taylor II, S. Washburn, R. Superfine, Thermally actuated untethered impact-driven locomotive microdevices. *Appl. Phys. Lett.* **89**, 203512 (2006).
30. H. Zeng, P. Wasylczyk, C. Parmeggiani, D. Martella, M. Burresi, D. S. Wiersma, Light-fueled microscopic walkers. *Adv. Mater.* **27**, 3883–3887 (2015).
31. S. Xu, Z. Yan, K.-I. Jang, W. Huang, H. Fu, J. Kim, Z. Wei, M. Flavin, J. McCracken, R. Wang, A. Badea, Y. Liu, D. Xiao, G. Zhou, J. Lee, H. U. Chung, H. Cheng, W. Ren, A. Banks, X. Li, U. Paik, R. G. Nuzzo, Y. Huang, Y. Zhang, J. A. Rogers, Assembly of micro/nanomaterials into complex, three-dimensional architectures by compressive buckling. *Science* **347**, 154–159 (2015).
32. M. Han, H. Wang, Y. Yang, C. Liang, W. Bai, Z. Yan, H. Li, Y. Xue, X. Wang, B. Akar, H. Zhao, H. Luan, J. Lim, I. Kandela, G. A. Ameer, Y. Zhang, Y. Huang, J. A. Rogers, Three-dimensional piezoelectric polymer microsystems for vibrational energy harvesting, robotic interfaces and biomedical implants. *Nat. Electron.* **2**, 26–35 (2019).
33. S. Han, S. Hong, J. Ham, J. Yeo, J. Lee, B. Kang, P. Lee, J. Kwon, S. S. Lee, M.-Y. Yang, S. H. Ko, Fast plasmonic laser nanowelding for a Cu-nanowire percolation network for flexible transparent conductors and stretchable electronics. *Adv. Mater.* **26**, 5808–5814 (2014).
34. H. Lee, H. Kim, I. Ha, J. Jung, P. Won, H. Cho, J. Yeo, S. Hong, S. Han, J. Kwon, K.-J. Cho, S. H. Ko, Directional shape morphing transparent walking soft robot. *Soft Robot.* **6**, 760–767 (2019).
35. A. Miriyev, K. Stack, H. Lipson, Soft material for soft actuators. *Nat. Commun.* **8**, 596 (2017).

36. S. I. Rich, R. J. Wood, C. Majidi, Untethered soft robotics. *Nat. Electron.* **1**, 102–112 (2018).

37. R. S. Pierre, W. Gosrich, S. Bergbreiter, A 3D-printed 1 mg legged microrobot running at 15 body lengths per second, in *Proceedings of the Solid-State Sensors, Actuators, and Microsystems Workshop*, SC (Hilton Head, 2018), vol. 3.

38. M. Switkes, B. L. Ervin, R. P. Kingsborough, M. Rothschild, M. Sworin, Retroreflectors for remote readout of colorimetric sensors. *Sens. Actuators B Chem.* **160**, 1244–1249 (2011).

39. H. Fu, K. Nan, W. Bai, W. Huang, K. Bai, L. Lu, C. Zhou, Y. Liu, F. Liu, J. Wang, M. Han, Z. Yan, H. Luan, Y. Zhang, Y. Zhang, J. Zhao, X. Cheng, M. Li, J. W. Lee, Y. Liu, D. Fang, X. Li, Y. Huang, Y. Zhang, J. A. Rogers, Morphable 3D mesostructures and microelectronic devices by multistable buckling mechanics. *Nat. Mater.* **17**, 268–276 (2018).

40. W. Pang, X. Cheng, H. Zhao, X. Guo, Z. Ji, G. Li, Y. Liang, Z. Xue, H. Song, F. Zhang, Z. Xu, L. Sang, W. Huang, T. Li, Y. Zhang, Electro-mechanically controlled assembly of reconfigurable 3D mesostructures and electronic devices based on dielectric elastomer platforms. *Natl. Sci. Rev.* **7**, 342–354 (2020).

41. K. Bai, X. Cheng, Z. Xue, H. Song, L. Sang, F. Zhang, F. Liu, X. Luo, W. Huang, Y. Huang, Y. Zhang, Geometrically reconfigurable 3D mesostructures and electromagnetic devices through a rational bottom-up design strategy. *Sci. Adv.* **6**, eabb7417 (2020).

42. M. Han, X. Chen, Code for the paper "Sub-millimeter scale multi-material terrestrial robots" (2022); 10.5281/zenodo.5839085.

43. L. C. Brinson, One-dimensional constitutive behavior of shape memory alloys: Thermomechanical derivation with non-constant material functions and redefined martensite internal variable. *J. Intell. Mater. Syst. Struct.* **4**, 229–242 (1993).

44. Y. Kim, H. Yuk, R. Zhao, S. A. Chester, X. Zhao, Printing ferromagnetic domains for untethered fast-transforming soft materials. *Nature* **558**, 274–279 (2018).

45. E. B. Joyee, Y. Pan, A fully three-dimensional printed inchworm-inspired soft robot with magnetic actuation. *Soft Robot.* **6**, 333–345 (2019).

46. S. Won, S. Kim, J. E. Park, J. Jeon, J. J. Wie, On-demand orbital maneuver of multiple soft robots via hierarchical magnetomotility. *Nat. Commun.* **10**, 4751 (2019).

47. S. Tottori, L. Zhang, F. Qiu, K. K. Krawczyk, A. Franco-Obregón, B. J. Nelson, Magnetic helical micromachines: Fabrication, controlled swimming, and cargo transport. *Adv. Mater.* **24**, 811–816 (2012).

48. K. Vollmers, D. R. Frutiger, B. E. Kratochvil, B. J. Nelson, Wireless resonant magnetic microactuator for untethered mobile microrobots. *Appl. Phys. Lett.* **92**, 144103 (2008).

49. D. Vogtmann, R. S. Pierre, S. Bergbreiter, A 25 MG magnetically actuated microrobot walking at > 5 body lengths/sec, in *Proceedings of the 2017 IEEE 30th International Conference on Micro Electro Mechanical Systems (MEMS)* (IEEE, 2017), pp. 179–182.

50. T. Li, G. Li, Y. Liang, T. Cheng, J. Dai, X. Yang, B. Liu, Z. Zeng, Z. Huang, Y. Luo, T. Xie, W. Yang, Fast-moving soft electronic fish. *Sci. Adv.* **3**, e1602045 (2017).

51. B. Goldberg, R. Zufferey, N. Doshi, E. F. Helbling, G. Whittredge, M. Kovac, R. J. Wood, Power and control autonomy for high-speed locomotion with an insect-scale legged robot. *IEEE Robot. Autom. Lett.* **3**, 987–993 (2018).

52. D. W. Haldane, R. S. Fearing, Running beyond the bio-inspired regime, in *Proceedings of the 2015 IEEE International Conference on Robotics and Automation (ICRA)* (IEEE, 2015), pp. 4539–4546.

53. X. Ji, X. Liu, V. Cacucciolo, M. Imboden, Y. Civet, A. E. Haitami, S. Cantin, Y. Perriard, H. Shea, An autonomous untethered fast soft robotic insect driven by low-voltage dielectric elastomer actuators. *Sci. Robot.* **4**, eaaz6451 (2019).

54. J. Li, Z. Liu, G. Huang, Z. An, G. Chen, J. Zhang, M. Li, R. Liu, Y. Mei, Hierarchical nanoporous microtubes for high-speed catalytic microengines. *NPG Asia Mater.* **6**, e94 (2014).

55. Z. Yan, M. Han, Y. Shi, A. Badea, Y. Yang, A. Kulkarni, E. Hanson, M. E. Kandel, X. Wen, F. Zhang, Y. Luo, Q. Lin, H. Zhang, X. Guo, Y. Huang, K. Nan, S. Jia, A. W. Oraham, M. B. Mevis, J. Lim, X. Guo, M. Gao, W. Ryu, K. J. Yu, B. G. Nicolau, A. Petronico, S. S. Rubakhin, J. Lou, P. M. Ajayan, K. Thornton, G. Popescu, D. Fang, J. V. Sweedler, P. V. Braun, H. Zhang, R. G. Nuzzo, Y. Huang, Y. Zhang, J. A. Rogers, Three-dimensional mesostructures as high-temperature growth templates, electronic cellular scaffolds, and self-propelled microrobots. *Proc. Natl. Acad. Sci. U.S.A.* **114**, E9455–E9464 (2017).

56. C. Huang, J.-a. Lv, X. Tian, Y. Wang, Y. Yu, J. Liu, Miniaturized swimming soft robot with complex movement actuated and controlled by remote light signals. *Sci. Rep.* **5**, 17414 (2015).

57. H. Zeng, O. M. Wani, P. Wasylczyk, A. Priimagi, Light-driven, caterpillar-inspired miniature inching robot. *Macromol. Rapid Commun.* **39**, 1700224 (2018).

58. M. Rogóż, H. Zeng, C. Xuan, D. S. Wiersma, P. Wasylczyk, Light-driven soft robot mimics caterpillar locomotion in natural scale. *Adv. Opt. Mater.* **4**, 1689–1694 (2016).

59. Y. Hu, G. Wu, T. Lan, J. Zhao, Y. Liu, W. Chen, A graphene-based bimorph structure for design of high performance photoactuators. *Adv. Mater.* **27**, 7867–7873 (2015).

60. H. Shahsavan, A. Aghakhani, H. Zeng, Y. Guo, Z. S. Davidson, A. Priimagi, M. Sitti, Bioinspired underwater locomotion of light-driven liquid crystal gels. *Proc. Natl. Acad. Sci. U.S.A.* **117**, 5125–5133 (2020).

61. C. Li, A. Iscen, H. Sai, K. Sato, N. A. Sather, S. M. Chin, Z. Álvarez, L. C. Palmer, G. C. Schatz, S. I. Stupp, Supramolecular-covalent hybrid polymers for light-activated mechanical actuation. *Nat. Mater.* **19**, 900–909 (2020).

62. Q. L. Zhu, C. Du, Y. Dai, M. Daab, M. Matejdes, J. Breu, W. Hong, Q. Zheng, Z. L. Wu, Light-steered locomotion of muscle-like hydrogel by self-coordinated shape change and friction modulation. *Nat. Commun.* **11**, 5166 (2020).

# Science Robotics

## Submillimeter-scale multimaterial terrestrial robots

Mengdi HanXiaogang GuoXuexian ChenCunman LiangHangbo ZhaoQihui ZhangWubin BaiFan ZhangHeming WeiChangsheng WuQinghong CuiShenglian YaoBohan SunYiyuan YangQuansan YangYuhang MaZhaoguo XueJean Won KwakTianqi JinQing TuEnming SongZiao TianYongfeng MeiDaining FangHaixia ZhangYonggang HuangYihui ZhangJohn A. Rogers

**View the article online**
https://www.science.org/doi/10.1126/scirobotics.abn0602
**Permissions**
https://www.science.org/help/reprints-and-permissions

Use of this article is subject to the Terms of service